

Filippo Casadei

Postdoctoral Fellow
Harvard University (SEAS),
Cambridge, MA 02138
e-mail: fcasadei@seas.harvard.edu

Katia Bertoldi¹

Professor
School of Engineering
and Applied Sciences (SEAS),
and Kavli Institute for Bionano Science,
Harvard University,
Cambridge, MA 02138
e-mail: bertoldi@seas.harvard.edu

David R. Clarke¹

Professor
School of Engineering
and Applied Sciences (SEAS),
Harvard University,
Cambridge, MA 02138
e-mail: clarke@seas.harvard.edu

Vibration Damping of Thermal Barrier Coatings Containing Ductile Metallic Layers

This paper explores the vibration damping properties of thermal barrier coatings (TBCs) containing thin plastically deformable metallic layers embedded in an elastic ceramic matrix. We develop an elastic–plastic dynamical model to study how work hardening, yield strain, and elastic modulus of the metal affect the macroscopic damping behavior of the coating. Finite element (FE) simulations validate the model and are used to estimate the damping capacity under axial and flexural vibration conditions. The model also provides an explanation for the widely observed nonlinear variation of the loss factor with strain in plasma-sprayed TBCs. Furthermore, it facilitates the identification of multilayer configurations that maximize energy dissipation. [DOI: 10.1115/1.4028031]

Keywords: thermal barrier coatings, vibration damping, metal layers

1 Introduction

TBCs have been extensively applied to provide thermal protection to superalloy structures in gas turbine engines, enabling higher turbine operating temperatures while preventing metal oxidation and hot corrosion [1–3]. While low-thermal conductivity oxides, such as yttria-stabilized zirconia (YSZ) and more recently gadolinium zirconate, are commonly used as refractory TBC materials, there is a growing interest in developing multifunctional configurations combining thermal protection and damping capabilities. Vibration damping is, in fact, critical for gas turbine blades that have to withstand high inertial stresses and repeated buffeting while operating at highly exacting temperatures and creep–fatigue conditions [4].

Damping is usually provided by extrinsic damping elements, but there is also interest in assessing and simulating the inherent dissipation properties of common oxide coating materials [5–10]. While these studies have mostly focused on internal friction damping and its functional dependence on the material microstructural features of bulk or as-deposited oxides, recently developed multilayer coatings comprising thin platinum (Pt) layers embedded into a ceramic (YSZ) matrix [11] may offer new opportunities for improved damping. Such TBCs combine materials with complementary thermomechanical properties to produce a multilayer coating with superior performance. For instance, thin Pt metal layers have the potential to reduce the radiative component of heat transport through the coating [11], while slowing the rate of oxide growth as well as potentially increasing the coating life [12,13]. The elastic and elastic–plastic behavior of such coatings under the effects of quasi-static loads has received some attention [12,13], but dynamic models that capture the hysteretic behavior of the system, and the associated energy dissipation mechanisms, have not been developed, and require a completely different analysis than those currently in use.

In this paper, we explore the vibration damping properties of multilayer coatings in which plastic straining of ductile metal layers dissipates energy through plasticity. We first develop a

simple damping model that correlates the damping capacity of a coating with the elastic–plastic properties of the ductile metal (Sec. 2). The model is also used to conduct parametric studies for different coating configurations. Then, in Sec. 3, we compare the results of the proposed model with FE simulations for both axial and flexural vibrations. Section 4 illustrates how the damping properties of a coating vary with temperature and shows how the damping model adopted in this study can be extended to capture a wider range of dissipation mechanisms commonly observed in TBCs.

2 Analytical Damping Model

Here, we focus on an elastic substrate of thickness H_s coated with a multilayer of thickness H comprising N metallic layers with thickness t_m embedded in an elastic matrix (see Fig. 1) and investigate analytically the damping capacity of the system under axial and flexural vibrations. The metal volume fraction $\Phi_m = (Nt_m)/H$ is used to define the volume of the metal relative to the overall thickness of the coating, and we assume that all the layers are uniformly spaced through the matrix as indicated in Fig. 1.

For the sake of simplicity, we only consider the contribution of the deformation in longitudinal direction, so that the elastic response of the substrate and matrix is fully captured by their Young's moduli E_s and E_c , respectively. Moreover, we assume that the metallic layers are characterized by an elastic–plastic response with linear kinematic hardening. This behavior is described by the elastic modulus E_m , the uniaxial yield stress σ_Y , and the tangent modulus $E_T = \gamma E_m$ in which $\gamma \in [0, 1]$ is a non-dimensional hardening coefficient, defining the slope of the stress–strain curve after yield (see Fig. 2(a)). A value of $\gamma = 0$ indicates an elastic–perfectly plastic behavior of the metallic layers, while $\gamma \rightarrow 1$ is the limit for a purely elastic material. When the metallic layers are strained beyond their yield point (i.e., $\varepsilon > \sigma_Y/E_m$), part of the elastic energy stored in the system (\mathcal{U}_{tot}) is dissipated by plastic work ($\Delta\mathcal{U}_{\text{tot}}$) in the metal. The macroscopic damping capacity of the system is quantified by the equivalent loss factor (Q^{-1}) defined as [14]

$$Q^{-1} \equiv \frac{1}{2\pi} \frac{\Delta\mathcal{U}_{\text{tot}}}{\mathcal{U}_{\text{tot}}} \quad (1)$$

¹Corresponding authors.

Contributed by the Applied Mechanics Division of ASME for publication in the JOURNAL OF APPLIED MECHANICS. Manuscript received May 22, 2014; final manuscript received July 8, 2014; accepted manuscript posted July 18, 2014; published online August 5, 2014. Editor: Yonggang Huang.

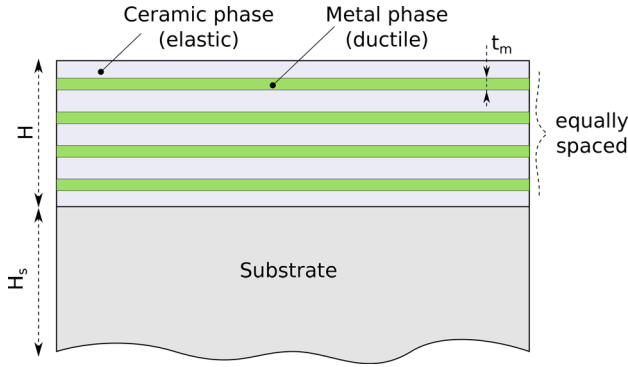


Fig. 1 Schematic of a coating comprising a planar stack of discrete ductile metal layers embedded in a ceramic matrix on an elastic substrate

When the system is subjected to cyclic loading, the energy per unit volume dissipated in one cycle by the metallic phase ($\Delta\mathcal{U}$) corresponds to the area enclosed by the hysteresis loop of the ductile material (see Fig. 2(b)) which, for the plasticity model considered here, is given by

$$\Delta\mathcal{U} = 2\sigma_Y 2\varepsilon_p \quad (2)$$

where ε_p denotes the plastic strain. Since

$$\varepsilon_p = \varepsilon - \varepsilon_e = \varepsilon - \frac{\varepsilon_Y E_m + \gamma E_m (\varepsilon - \varepsilon_Y)}{E_m} \quad (3)$$

$\varepsilon_Y = \sigma_Y / E_m$ being the yield strain, Eq. (2) can be rewritten as

$$\Delta\mathcal{U} = 4\varepsilon_Y (\varepsilon - \varepsilon_Y) (1 - \gamma) E_m \quad (4)$$

The energy dissipated by the coating in one cycle ($\Delta\mathcal{U}_{\text{tot}}$) is then obtained by integrating Eq. (2) over the volume of the ductile material

$$\Delta\mathcal{U}_{\text{tot}} = \sum_{i=1}^N \int_0^L \int_{z_b^i}^{z_t^i} \Delta\mathcal{U} w \, dz \, dx \quad (5)$$

in which L and w are the length and width of the N ductile layers, and z_b^i and z_t^i are the bottom and top coordinates of the i th layer, respectively (see Fig. 3(c)).

2.1 Dissipation Under Axial Vibrations. First, we consider the case of axial vibrations induced by a longitudinal harmonic force $F = F_0 \sin(\omega t)$ (see Fig. 3(a)) and resulting in a tip

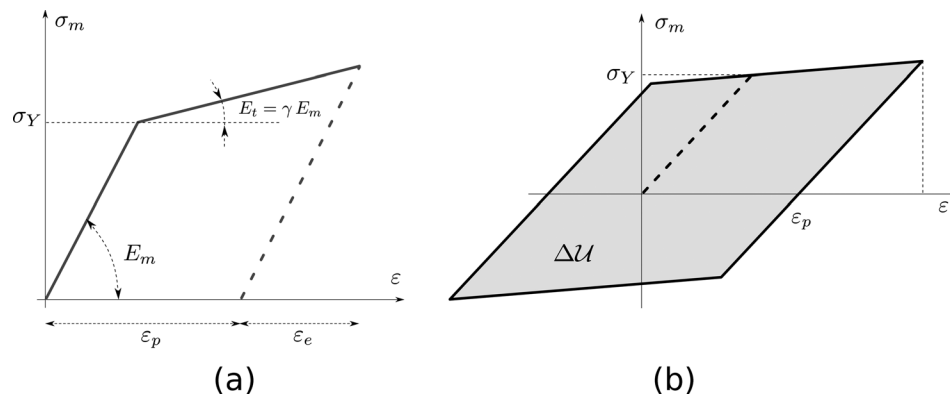


Fig. 2 Elastic-plastic constitutive law of the ductile metal (a) and schematic of the cyclic behavior (b)

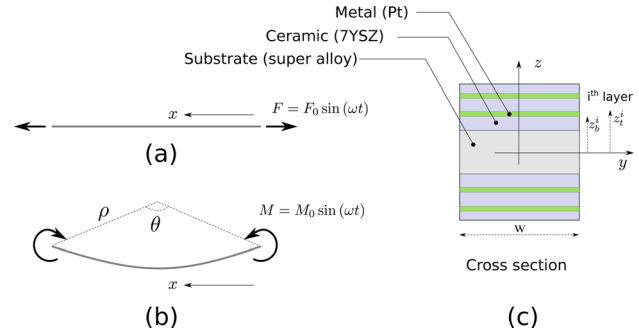


Fig. 3 Schematic of the beam undergoing axial (a) and flexural deformations (b), and its cross section (c)

displacement with amplitude u_0 . In this case, both the elastic substrate and all the layers of the coating are subjected to a homogeneous state of longitudinal strain, which varies harmonically and has amplitude $\varepsilon = u_0/L$. Therefore, Eq. (4) simplifies to

$$\Delta\mathcal{U}_{\text{tot}} = (EA)_m L \varepsilon_Y (\varepsilon - \varepsilon_Y) (1 - \gamma) \quad (6)$$

where $(EA)_m = w \sum_{i=1}^N E_i (z_t^i - z_b^i)$ denotes the axial stiffness of the metallic phase.

Furthermore, the strain energy stored in one cycle by the system is approximated as [15]

$$\mathcal{U}_{\text{tot}} = \frac{1}{2} \frac{(EA)_e + (EA)_m}{L} u_0^2 \quad (7)$$

where $(EA)_e$ is the contributions from the elastic materials (ceramic and superalloy) to the axial stiffness of the beam. Substituting Eqs. (6) and (7) into Eq. (1) gives

$$Q^{-1} = \frac{4}{\pi} \frac{(\varepsilon - \varepsilon_Y) \varepsilon_Y}{\varepsilon^2} \frac{(1 - \gamma)}{1 + (EA)_e / (EA)_m} \quad (8)$$

which can be rearranged as

$$Q^{-1} = \frac{4}{\pi} \frac{(\mu - 1)(1 - \gamma)}{\mu^2} \frac{1}{1 + r^2} \quad (9)$$

by letting $\mu = \varepsilon / \varepsilon_Y$ and $r^2 = (EA)_e / (EA)_m$. Note that in the absence of the substrate r^2 simplifies to $r^2 = E_c (1 - \Phi_m) / E_m \Phi_m$.

Analysis of Eq. (9) reveals that the energy dissipation properties of the system under consideration are remarkably similar to the one proposed for a bilinear hysteretic springs-mass oscillator [15]. Therefore, the response of the system can be described by an

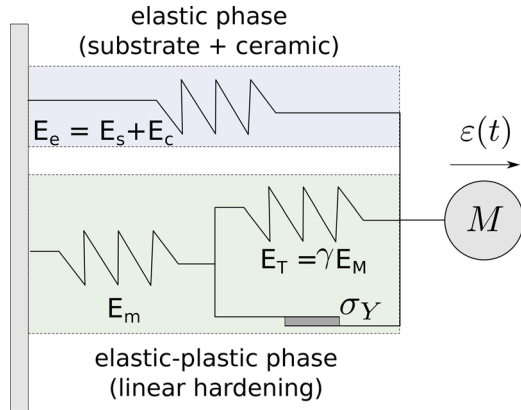


Fig. 4 Schematic of the equivalent SDOF model of the system. The substrate and ceramic elastic moduli, although different, are combined into a single elastic stiffness term E_e , while E_m is the linear stiffness of the metal. Also, E_T and σ_Y denote the hardening modulus and yield stress of the metal, respectively.

equivalent single-degree-of-freedom (SDOF) model as shown in Fig. 4, consisting of an elastic–plastic spring (to account for the metallic layers) connected in parallel to an elastic spring (to account for the elastic matrix and substrate).

In Fig. 5, we report the evolution of Q^{-1} as a function of the deformation amplitude $\mu = \varepsilon/\varepsilon_Y$ for different values of the hardening parameter (γ). Only values of μ greater than unity (i.e., $\mu > 1$) are considered since no plasticity and hence no hysteresis takes place below this limit. Both the analytical predictions provided by Eq. (9) (continuous lines) and numerical results obtained by computing the steady state response of the equivalent SDOF nonlinear model (see Fig. 4) for forced harmonic motion (markers—see the Appendix for details) are reported, showing excellent agreement.

As expected, the results in Fig. 5 indicate that damping is enhanced when the metallic layers behave as elastic–perfectly plastic materials, with no strain hardening after yield (i.e., $\gamma \rightarrow 0$). In fact, for a given applied strain, lower values of γ increase the area of the hysteresis loop, which in turn results in higher dissipation of mechanical energy by plastic work. Furthermore, Fig. 5 reveals that the coating loss factor does not monotonically increase with μ and that it is characterized by a maximum peak occurring when $\varepsilon = 2\varepsilon_Y$. The presence of a maximum damping capacity in Fig. 5 may have important implications for the dynamic design of multilayer coatings, since it defines an optimal value of the applied deformation that maximizes Q^{-1} .

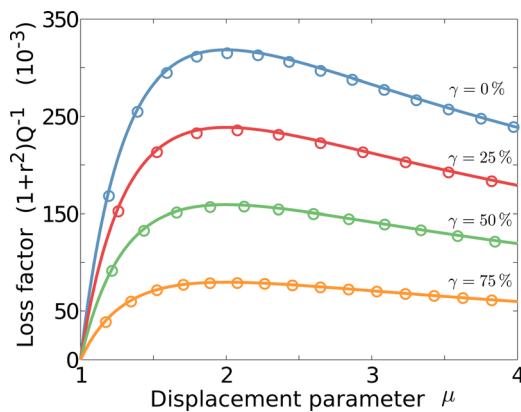


Fig. 5 Functional variation of the effective loss factor on the deformation (μ) for different values of the kinematic hardening parameter γ . Analytical solution (solid lines) and numerical solution (\circ markers).

2.2 Dissipation Under Flexural Vibrations. Under the effect of two bending moments M applied at the two ends (see Fig. 3(b)), the structure is subjected to a uniform strain distribution in the longitudinal direction [16]

$$\varepsilon = \frac{z}{\rho} = \theta \frac{z}{L} \quad (10)$$

where z represents the vertical distance of a point from the centroid of the cross section (Fig. 3(c)), θ is the cross-sectional rotation, and $\rho = L/\theta$ is the radius of curvature of the neutral axis (see Fig. 3(b)). Therefore, a point in a metallic layer located at a distance z from the centroid yields when a critical value θ_Y is reached such that

$$\theta_Y = \varepsilon_Y \frac{L}{z} = \frac{\sigma_Y L}{E_m z} \quad (11)$$

Substituting Eqs. (10) and (11) into Eq. (4) and integrating over the volume leads to

$$\begin{aligned} \Delta \mathcal{U}_{\text{tot}} &= \sum_{i=1}^{N_Y} 4E_m (z_i^3 - z_b^3) \frac{\theta_Y (\theta - \theta_Y)}{L} (1 - \gamma) \\ &= 4(EI)_m \frac{\theta_Y (\theta - \theta_Y)}{L} (1 - \gamma) \end{aligned} \quad (12)$$

where

$$(EI)_m = \frac{1}{3} \sum_{i=1}^{N_Y} E_m [(z_i^3) - (z_b^3)] \quad (13)$$

is the bending stiffness of the N_Y metal layers for which the strain is larger than the metal yield strain. Equation (13) is clearly a nonlinear function of the applied deformation θ which determines how many layers (N_Y) undergo plastic deformations. Note that, for the sake of simplicity, in Eq. (13), we use a discrete summation symbol even though in our calculations we consider also contributions from layers that are only partially in the plastic range. Interestingly, Eq. (13) can be approximated by extending the summation to all the (N) metal layers as

$$(\hat{EI})_m = \frac{1}{3} \sum_{i=1}^N E_m [(z_i^3) - (z_b^3)] \quad (14)$$

so that the dependence on the deformation θ is eliminated by assuming that all the metal layers yield simultaneously, while contributing to dissipate energy according to their relative location on the cross section.

The effective viscous damping of the system is obtained by dividing Eq. (12) by the elastic energy stored by the beam (\mathcal{U}_{tot}) in one cycle of steady state vibrations, namely,

$$\mathcal{U}_{\text{tot}} = \frac{1}{2} \frac{(EI)_e + (\hat{EI})_m}{L} \theta^2 \quad (15)$$

where $(EI)_e$ is the bending stiffness of the elastic phase (ceramic and superalloy). Substituting Eqs. (12) and (15) into Eq. (1) gives

$$Q^{-1} = \frac{4(\theta - \theta_Y)\theta_Y}{\pi \theta^2} \frac{(1 - \gamma)}{1 + (EI)_e / (EI)_m} \quad (16)$$

which can be cast as in Eq. (9) by letting $\mu = \theta/\theta_Y$ and $r^2 = (EI)_e / (EI)_m$. Equation (16) can be further simplified by making use of the approximation introduced in Eq. (14), yielding

$$\hat{Q}^{-1} = \frac{4(\theta - \theta_Y)\theta_Y}{\pi \theta^2} \frac{(1 - \gamma)}{1 + (EI)_e / (\hat{EI})_m} \quad (17)$$

In Fig. 6(d), we compare the predictions for energy dissipated using the exact (Eq. (16)) and approximate (Eq. (17)) expressions derived above for three configurations characterized by the cross section shown in Figs. 6(a)–6(c). Each cross section comprises a substrate of thickness $H_s = 6$ mm, coated on both sides by a multi-layer of thickness $H = 1$ mm with $N = 2, 3$, and 4 metallic layers of thickness $t_m = 0.1$ mm. Furthermore, we assume the substrate and elastic matrix to be characterized by Young's moduli $E_s = 120$ GPa and $E_e = 22$ GPa, respectively, and the metallic layers to be made of an elastic–perfectly plastic material (i.e., $\gamma = 0$) with $E_m = 164.6$ GPa and $\sigma_Y = 185$ MPa [17].

Remarkably, the results presented in Fig. 6(d) indicate that the exact (Eq. (16)) and approximate (Eq. (17)) expressions lead to very similar results, with some discrepancies observed for values of μ close to unity. In this range, in fact, the exact model (Eq. (16)) accounts for the fact that not all the layers undergo plastic deformations at the same time, thus predicting a slightly smaller dissipation than the approximate model. When all the metal layers operate in the plastic regime (i.e., for slightly higher values of $\mu \sim 1.5$), the two models are exactly equivalent. From this, it is possible to conclude that the equivalent SDOF model shown in Fig. 4 can also be adopted to represent the dissipation of a multi-layer undergoing flexural motion. This is achieved by properly replacing the stiffness of the two springs with the bending stiffnesses of the elastic and ductile materials.

Next, we exploit the approximate model to investigate the effects of parameters that may be of interest for the design of multifunctional coatings. In particular, we focus on a coating with thickness $H = 200$ μ m, two equally spaced ductile layers (see Fig. 7—right inset), whose relative metal volume fraction (Φ_m) is parametrically varied, and investigate the combinations of metal volume fraction (Φ_m) and substrate thickness (H_s) that maximize energy dissipation. Figure 7 shows how the maximum damping capacity of the considered configuration (i.e., $\max_{\mu} Q^{-1}(\mu)$ —

subsequently this will also be referred to as the damping peak) changes as a function of Φ_m .

While results shown in Fig. 7 confirm that increasing the volume of plastically deformable material will result in higher values of energy loss, it remains unclear whether it is more effective to incorporate multiple thin ductile layers or to increase the thickness of each layer while limiting their number. This question is addressed in Fig. 8 where results for different volume fractions obtained by increasing either the number of layers or the thickness of a single layer (see Fig. 8—right inset) are compared. Interestingly, this study reveals that despite some minor differences at low values of the H_s/H ratio, damping is not particularly sensitive on the arrangement of the metal layers used to achieve a particular value of Φ_m . The axial strain achieved in the ductile layers due to bending is, in fact, dictated by their offset from the sectional centroid of the beam which is mostly affected by the substrate thickness rather than the spacing between the individual layers. This result therefore suggests that either the number of layers or their individual thickness can be chosen to maximize other properties such as delamination resistance or thermal protection.

3 Comparison With FE Results

3.1 Overview of the Model. FE simulations are conducted with the commercial code ABAQUS/Standard to validate the analytical predictions presented above. In particular, we focus on the configuration shown in Fig. 9, consisting of a superalloy substrate (PWA-1484) coated by a 7% YSZ (7YSZ) oxide with embedded Pt layers. The beam features length $L = 100$ mm, topcoat thickness $H = 200$ μ m of which the relative metal volume fraction is parametrically varied. The effect of the substrate thickness (H_s) is also investigated as an independent parameter. To avoid any coupling between axial and bending deformations, the substrate is coated on both sides. The system is discretized using quadrilateral plane-stress elements (CPS4 elements in ABAQUS) and the accuracy of the mesh has been ascertained through a refinement study. As shown in Fig. 9, the system is not constrained and is loaded by a set of self-equilibrating forces applied at the two ends. Specifically, axial motion is achieved by applying a concentrated nodal force at the centroid of the cross section, while pure bending is obtained by means of two equal nodal forces (with opposite directions) applied at the top and bottom of the left and right cross sections (Fig. 9(b)). The loads are varied harmonically in time, and the response is computed up to steady state using the implicit time marching scheme implemented into ABAQUS/Standard. The energy dissipated per cycle at steady state is estimated from the computed results as described in the Appendix.

A summary of the elastic material properties considered in this study is presented in Table 1. These values are used throughout the rest of this work unless otherwise specified. Note, the elastic modulus and density values listed correspond to those of YSZ coating rather than fully dense zirconia which has a significantly higher elastic modulus. Furthermore, Pt is modeled as an elastic–plastic material with linear kinematic hardening, a yield stress $\sigma_Y = 185.0$ MPa [17], and its hardening modulus is expressed in terms of the linear elastic modulus through a hardening parameter $\gamma \in [0, 1]$.

3.2 Axial Vibrations. We first investigate the case in which the beam is loaded by an axial force located at the centroid of the tip cross section. For the sake of clarity, here, we focus on a configuration with a single metal layer, but similar results have been obtained for configurations involving multiple layers. For a direct comparison with the damping predicted by the analytical model presented above, simulations are conducted by assuming that the mass of the model is concentrated at the tip central node (where the force is applied). Damping is then calculated by integrating the transient response up to steady state when the external force

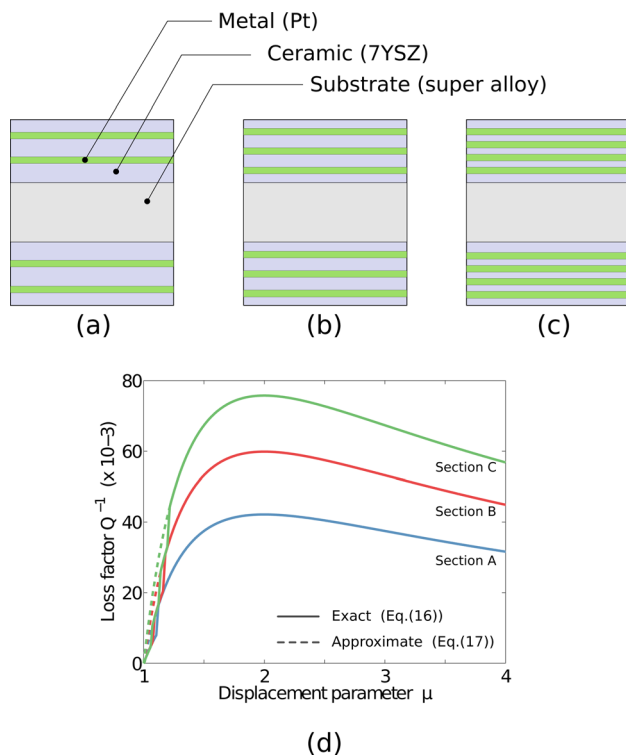


Fig. 6 Schematic of three cross sections (labeled A, B, and C, respectively) used to estimate the damping of the system in bending ((a)–(c)). Comparison between the loss factor of the three sections computed with the exact and approximate damping models (d).

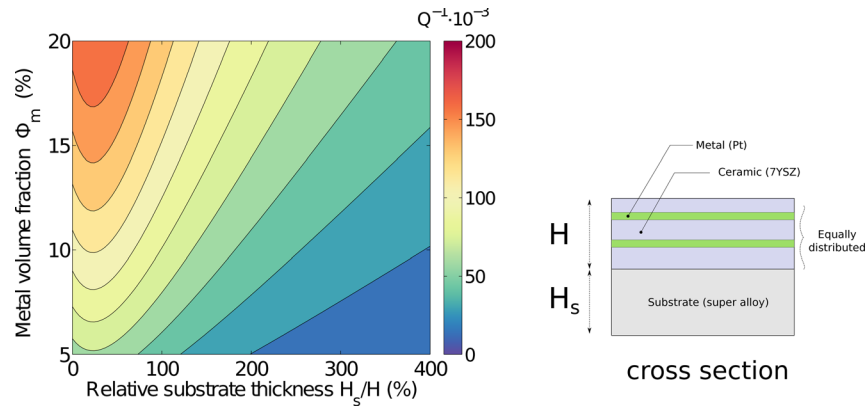


Fig. 7 Variation of the maximum damping capacity of a coating comprising two ductile layers as a function of the substrate thickness (H_s) and metal volume fraction (Φ_m)

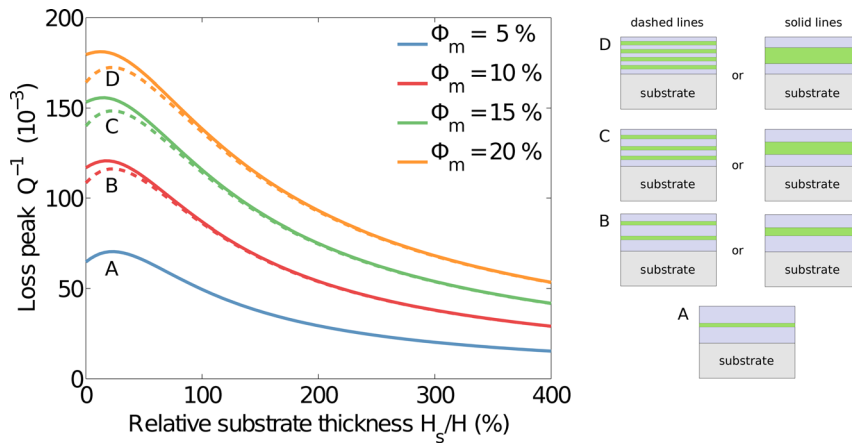


Fig. 8 Variation of the damping peak for different values of the substrate thickness (H_s). This study compares results for different volume fractions obtained by increasing either the number of layers from one to four as shown on the side (dashed lines) or the thickness of a single layer (solid lines).

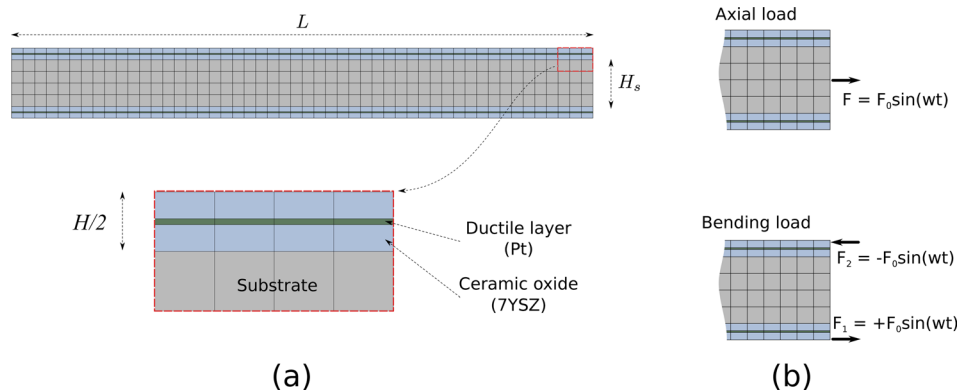


Fig. 9 FE discretization of an elastic superalloy coated on both sides by a 7YSZ ceramic containing a ductile metal layer (a) and detail of the applied axial and bending loads (b)

Table 1 Material properties used in the FE model

	Density (kg/m ³)	Elastic modulus (GPa)	Poisson's ratio
7YSZ	4930	22.0	0.35
Platinum	21,450	164.6	0.39
PWA-1484	8700	120.0	0.35

varies harmonically at the axial resonance frequency of the system.

Results of this analysis are presented in Fig. 10 which also includes the damping predicted by the FE model assuming uniform density distribution. Specifically, Fig. 10 shows that the damping predicted by the analytical model (i.e., Eq. (8)) for various combinations of the system's parameters is in excellent agreement with the one predicted by the FE model with concentrated

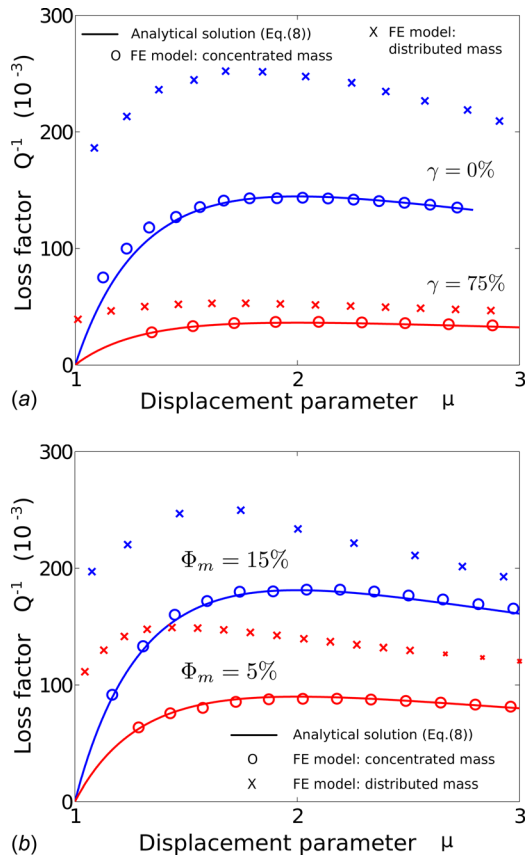


Fig. 10 Comparison between analytical and FE predictions of the energy dissipation in the coating for different values of the hardening parameter γ ($\Phi_m = 10\%$) (a) and metal volume fraction Φ_m ($\gamma = 0.0$) (b)

mass. It is however interesting to note that, for a prescribed level of axial strain, the total damping capacity calculated by the FE model with uniform mass distribution is significantly higher than the one calculated by Eq. (8). The distributed inertia forces, in fact, give rise to higher and nonuniform axial stresses that remarkably enhance energy dissipation. For example, Fig. 10 reveals that, contrary to the analytical model, nonzero damping is present even when the system is strained at or below its macroscopic yield limit ($\mu < 1$).

This behavior is further illustrated by comparing contours of the axial stress field in the beam (S11) obtained at the peak of steady state vibrations. For instance, results shown in Fig. 11 show that when the beam has concentrated mass (Fig. 11(a)), the ceramic and metal phases feature uniform, albeit distinct, values of axial stress as predicted by the spring-mass model introduced in Sec. 2. However, when the actual mass distribution of the two materials is considered (Fig. 11(b)), the distributed inertia forces at resonance generate non uniform axial stresses which strain the

ductile layer beyond its yield limit even when the overall strain is below the $\mu = 1$ limit.

The FE model considered in this section is also exploited to investigate the effect of the substrate on energy dissipation. A concise, yet meaningful, understanding of the behavior of the system is obtained by computing the variation of the damping peak as a function of the relative substrate thickness (H_s/H). Analyses are conducted for a reference configuration with metal volume fraction $\Phi_m = 10\%$, an elastic-perfectly plastic hardening law ($\gamma = 0$), and uniformly distributed density of the three materials. Analysis of Eq. (8) suggests that the damping capacity of the system rapidly decays when $H_s \neq 0$ (r^2 being at the denominator of Eq. (8)) and that it tends to zero at the limit when $H_s \rightarrow \infty$. This trend is clearly shown by both analytical and numerical results in Fig. 12 where the loss factor has been normalized to its initial value ($Q^{-1}(H_s = 0)$) to compensate for the discrepancy induced by the distributed mass effect.

3.3 Flexural Vibrations. The aerodynamic loads acting on turbine blades mostly excite their bending modes of deformation. It is therefore important to predict the amount of damping that is provided by the present configuration during flexural vibrations. The energy loss predicted by Eq. (16) is validated by means of FE simulations using the FE model previously adopted for axial vibrations. The beam is excited by a concentrated moment applied at the two ends of the beam as shown in Fig. 9(b). A first comparative study is conducted by considering a 7YSZ coating comprising two Pt-rhodium layers equally distributed through the cross section with a volume fraction $\Phi_m = 10\%$. Guided by our previous results on axial vibrations, we investigate both the case in which the structure features homogeneous (uniform) density distribution and the one in which the mass is concentrated at the beam tip.

Results of this analysis are shown in Fig. 13 in which the damping capacity of the system is evaluated for different values of the displacement parameter (μ) and hardening modulus (γ). The damping predicted by the model (Eq. (16)) is in excellent agreement with the FE results with lumped mass, while only minor discrepancies are observed when considering the actual density distribution. Also, contrary to the case of axial vibrations, the effect of the distributed inertia forces does not seem to play an important role. This conclusion is further corroborated by results illustrated in Fig. 14 showing a virtually identical distribution of the axial stress (S11) in the FE model with and without distributed mass.

Furthermore, Fig. 13 shows that the coating damping capacity is characterized by a distinct peak at $\mu = 2$ before decreasing again, as well as the expected dependency on the hardening modulus (γ). Interestingly, Fig. 13 also indicates that when the system is loaded in bending, its damping capacity is less than that observed for the case of axial vibrations (see Fig. 10). This behavior is attributed to the linear variation of the axial strain through the cross section which leads to smaller volume under plastic strain as opposed to the uniform strain distribution that characterizes the longitudinal motion of the beam.

The effect of an elastic substrate, typically made of a nickel-based superalloy, such as PWA-1484, on the damping capacity is

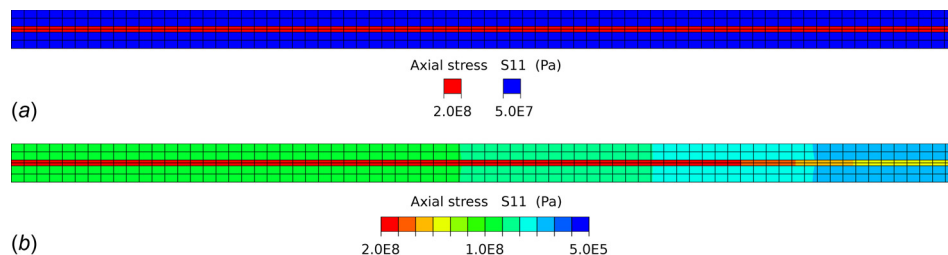


Fig. 11 Steady state axial stress distribution (S11) in the beam without distributed mass (a) and with distributed mass (b)

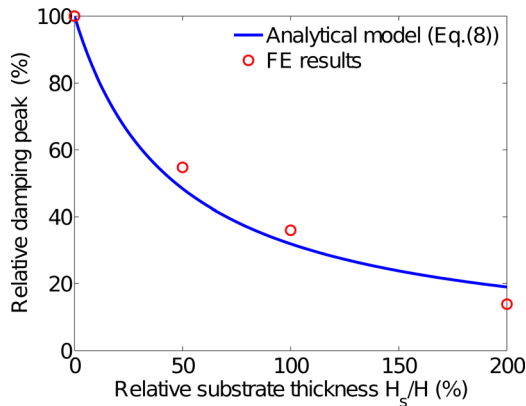


Fig. 12 Variation of the relative damping peak ($Q^{-1}/Q^{-1}(H_s=0)$) as a function of the substrate thickness (H_s) ($\Phi_m = 10\%$)

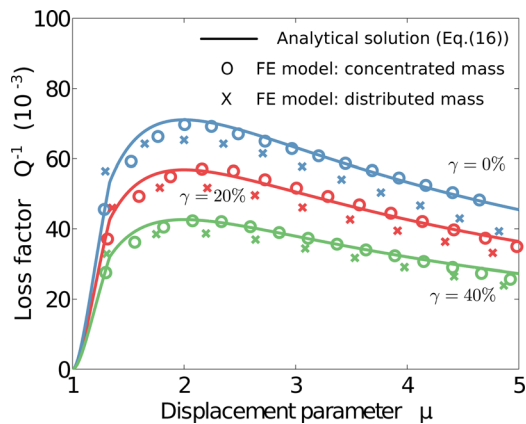


Fig. 13 Variation of the effective loss factor on the bending displacement parameter μ , for different values of the hardening parameter γ (coating only)

also investigated by parametrically varying the substrate thickness (H_s). Both analytical and numerical results are obtained for a model configuration featuring metal volume fraction $\Phi_m = 10\%$, and an elastic-perfectly plastic constitutive law for the metal (i.e., $\gamma = 0$). Results of this study are presented in Fig. 15 which again shows excellent agreement between the analytical and FE solutions. Interestingly, results show a peculiar trend characterized by an initial increase of damping for small values of the H_s/H ratio

followed by a monotonic decrease. This trend, which is also shown in Fig. 8, is the result of two competing effects associated with the substrate thickness. First, increasing the distance between the ductile layers and the centroid results in both higher strains and damping. Second, it also increases the elastic strain energy stored per cycle. Because of this, the percent decrease in energy loss (see Eq. (1)) is not as pronounced as in the case of axial vibrations.

4 Discussion

4.1 Variation of Damping With Temperature. As many materials' properties, such as yield stress and modulus, vary with temperature, it is critical to gain insights into the combination of these parameters that maximize energy dissipation at intermediate as well as high temperatures. Interestingly, the functional dependence of damping on temperature (T) can be straightforwardly investigated using the current model by incorporating the temperature variation of the metal elastic modulus (E_m) and yield stress (σ_Y) into Eq. (16) or Eq. (8).

Unfortunately, little is known about the high temperature properties for Pt—or indeed many other candidate metals, but some data on a Pt-10% rhodium (Pt-10%Rh) alloy are available from experiments conducted over a limited temperature range [17,18]. For this work, the data have been extrapolated to other temperatures using a low-order polynomial function, as shown in Fig. 16.

As an illustration of the effect of temperature, the variation of a coating damping capacity with temperature is computed for axial deformations using Eq. (8) for a coating comprising a ceramic matrix ($E_c = 22.0$ GPa) and a Pt-10%Rh alloy layer with $\Phi_m = 10\%$ and $\gamma = 10\%$. For a given value of applied strain (ϵ), the loss factor (Q^{-1}) is evaluated by neglecting, for simplicity, the dependence of E_c on temperature, while accounting for the temperature variation of the metal modulus $E_m = E_m(T)$ and yield stress $\sigma_Y = \sigma_Y(T)$ taken from Fig. 16. Figure 17 shows that the resulting variation of Q^{-1} with temperature has different trends depending on the specific strain imposed. For example, at small values of ϵ , damping is observed only above a temperature at which the yield stress diminishes to allow for plastic deformations to take place in the system. At higher strains, the loss factor features a distinct peak at temperatures corresponding to values of the metal yield stress that maximize Eq. (8) (i.e., for which $\mu \approx 2$). The dependence of such peak temperature on the materials comprising the coating is shown in Fig. 18. This is most simply investigated by scaling the metal modulus by a constant α_E while keeping the yield stress constant, or, alternatively, by scaling the yield stress by a factor α_σ . Interestingly, the results show that metals with lower elastic moduli are characterized by higher peak temperatures (see Fig. 18(a)) as well as lower damping. A smaller modulus, in fact, leads to lower stresses in the metal layer so that a

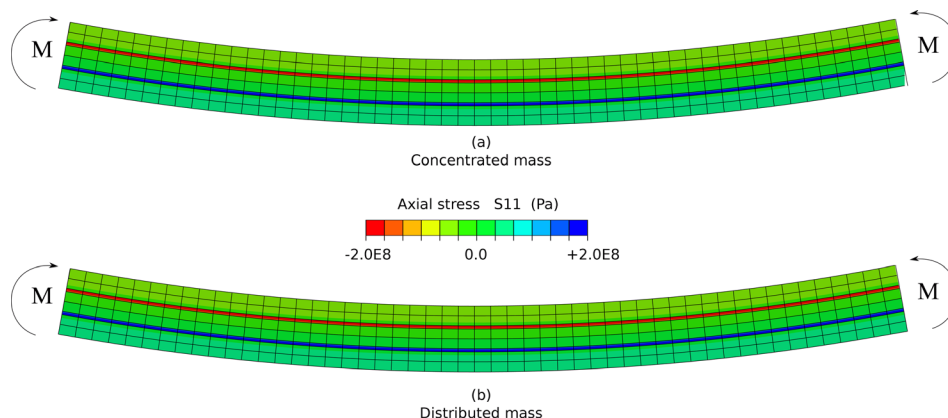


Fig. 14 Comparison of the steady state axial stress distribution (S11) in the beam with mass concentrated at the tip (a) and with distributed mass (b)

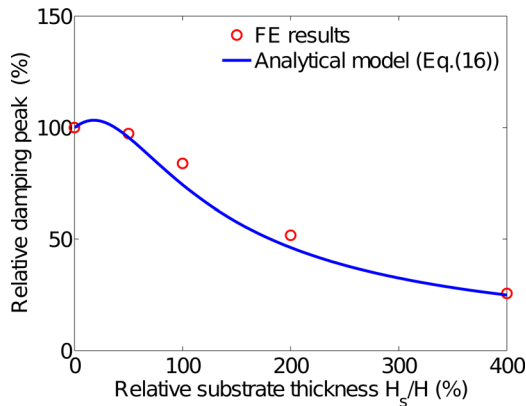


Fig. 15 Variation of the relative damping peak ($Q^{-1}/Q^{-1}(H_s=0)$) as a function of the substrate thickness (H_s) ($\Phi_m = 10\%$)

correspondingly smaller yield stress, i.e., higher temperature, is needed for the metal to reach its yield stress and deform plastically. Also, Fig. 18(b) indicates that the metal yield stress significantly affects the damping peak temperature without appreciably changing the maximum damping capacity of the system.

To guide the selection of coating materials, a concise yet meaningful measure of a coating damping performance is needed. We propose a damping efficiency (η_T)

$$\eta_T(\varepsilon) = \frac{1}{T_2 - T_1} \int_{T_1}^{T_2} \frac{Q^{-1}(\varepsilon, T)}{Q_{\text{peak}}^{-1}(\varepsilon)} dT \quad (18)$$

defined as the ratio between the average damping observed over a temperature range $[T_1, T_2]$ of interest and the corresponding damping peak $Q_{\text{peak}}^{-1} = \max_{T \in [T_1, T_2]} Q^{-1}(T)$. Here, the damping efficiency of the YSZ-Pt coating described above is computed over an arbitrary temperature range, in this case, between $T_1 = 0(\text{C})$ and $T_2 = 1500(\text{C})$ for different strains. As shown in Fig. 19, this parameter identifies a combination of elastic and plastic properties that maximizes the (average) damping capacity of a coating given an expected deformation level.

4.2 Extension to Other Dissipation Mechanisms. A characteristic feature of the predicted energy dissipation is the nonlinear variation of the loss factor with strain, peaking at a strain corresponding to $\mu = 2$ before decreasing at larger strains. Strikingly, this same damping behavior has been reported for plasma-sprayed coatings and attributed to friction due to relative movement of the faces of microcracks within plasma-sprayed coatings or possible sliding of the columnar microstructure commonly obtained with

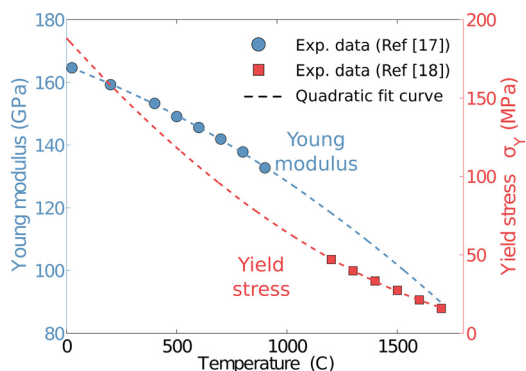


Fig. 16 Variation of the elastic modulus and yield stress of a Pt-10%Rh alloy with temperature

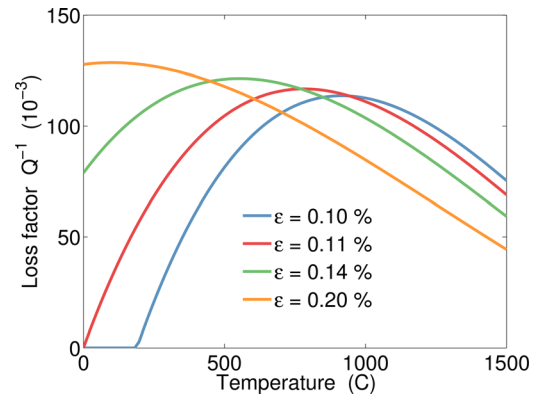


Fig. 17 Variation of the coating damping capacity with temperature for different values of the applied axial strain (i.e., Eq. (8))

vapor deposition techniques [7–9,19,20]. This suggests that the present model, although introduced to describe the effects of metal plasticity on damping, can also describe a broader class of dissipative phenomena observed in coatings. For instance, the elastic-plastic behavior of the materials used in our model (see Fig. 4) can be replaced by constitutive laws describing the nonlinear energy loss induced by frictional motion between microstructural features.

As a quantitative example, we consider the empirical friction model originally proposed by Dahl [21], which is widely adopted because of its simplicity and its ability to capture a broad variety of hysteretic friction phenomena. According to this model, the friction force (F_H) is a hysteretic function (without memory) of the displacement (x) which can be expressed as

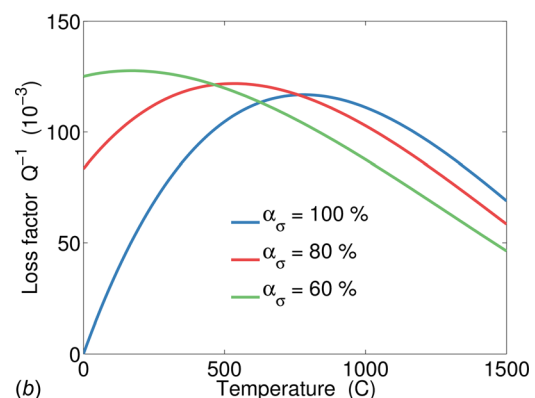
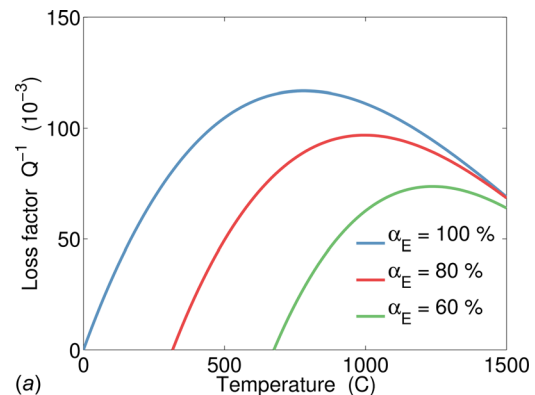


Fig. 18 Influence of the metal modulus (a) and yield stress (b) of a coating with 10% metal on the variation of damping with temperature for a given deformation ($\varepsilon = 0.11\%$)

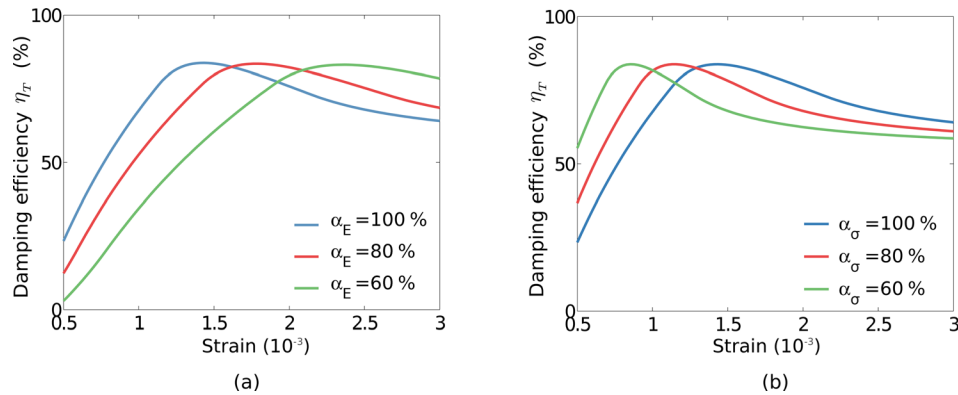


Fig. 19 Influence of the metal modulus (a) and yield stress (b) on the variation of damping efficiency η_T (see Eq. (18)) with strain

$$\frac{dF_H(x)}{dx} = k \left| 1 - \frac{F_H}{F_c} \text{sign}(\dot{x}) \right|^\alpha \text{sign} \left(1 - \frac{F_H}{F_c} \text{sign}(\dot{x}) \right) \quad (19)$$

where k is the slope of the force–deflection curve at $F_H=0$, F_c is the friction force at “yield” or the kinetic friction force, and α defines the slope. At the steady state limit (i.e., when $F_H=F_c$), dF_H/dx goes to zero, and Dahl’s model coincides with the Coulomb model.

Equation (19) can be used to replace the bilinear elastic–plastic behavior adopted in the equivalent SDOF model shown in Fig. 4, and the loss factor can be estimated from the computed steady state response as was carried out to estimate Q^{-1} in Sec. 2. Results of this analysis are presented in Fig. 20 which shows how the variation of damping (Q^{-1}) with strain remarkably resembles the trend previously observed for the bilinear hysteretic system. It is also important to notice that the frictional damping, shown in Fig. 20, is observed from the onset of motion (i.e., when $\mu \neq 0$) and not only after a yield value as in the ductile layers cases previously considered.

4.3 Damping Magnitude. In the foregoing calculations, the magnitude of the damping loss, Q^{-1} , has been of the order of 10–100 times 10^{-3} , comparable to measurements reported of the damping of zirconia coated superalloy beams up to about 1000 °C [6]. However, this is a coincidence, since the damping mechanisms are quite different. The magnitude of the damping calculated in this work is set by the ratio of the elastic modulus of the zirconia to that of the metal, the term r^2 in Eq. (9). Because of the columnar and porous microstructures of the zirconia coatings used for thermal protection, the zirconia elastic modulus is much lower than that of fully dense zirconia (approximately 20 GPa versus

240 GPa). Consequently, the calculated damping loss is higher than would be achieved if the coating was a fully dense zirconia. In addition, while the model explicitly considers multilayer metal–ceramic coatings, existing commercial zirconia coatings also contain a thin metal bond-coat between the zirconia layer and the superalloy underneath. Hitherto, the effect of this metal layer, typically NiAl or a NiAlCrY alloy, on damping has been neglected. Unfortunately, the composition of the bond-coat alloy changes by interdiffusion and so the yield stresses are not unique. However, with appropriate data, the model presented in this work could be extended to specifically include contribution from plastic deformation in the bond-coat.

5 Conclusions

An elastic–plastic dynamical model is introduced to assess the potential of metal–ceramic layered TBCs to provide vibration damping as well as thermal protection. The model takes into account the effect of yield strain, elastic moduli, and work hardening of the metal on the macroscopic damping behavior and allows for damping to be predicted for a variety of axial and flexural vibration conditions. Comparison with FE results shows that the model provides accurate results that can be exploited for parametric design and optimization studies.

Finally, we observe that, although introduced to describe the effects of metal plasticity on damping, the present approach can be generalized to include a widely used generic friction law that captures the nonlinear energy loss with flexural strain consistently observed in plasma-sprayed coating systems.

Acknowledgment

The authors would like to acknowledge partial support for this work through a subcontract from DVTI under an SBIR Contract No. FA8650-10-M-2208 from the Air Force Research Laboratories.

Appendix

Governing Equations of the Equivalent SDOF System

The dynamic equilibrium equation of the equivalent SDOF model shown in Fig. 4 are given by

$$M\ddot{\varepsilon}(t) + \sigma(t) = f(t) \quad (A1)$$

where $\varepsilon(t)$ denotes the time dependent displacement of the mass induced by the externally applied force $f(t)$. Also, in Eq. (A1), $\sigma(t)$ is a nonlinear restoring force given by the sum of the contributions of the elastic (σ_e), and ductile (σ_m) springs as

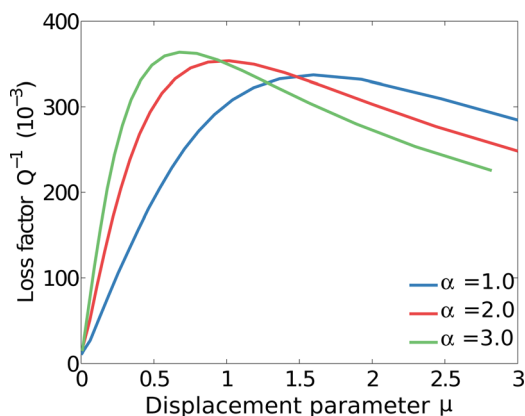


Fig. 20 Variation of the loss factor associated with the Dahl frictional law computed for different values of the parameter α

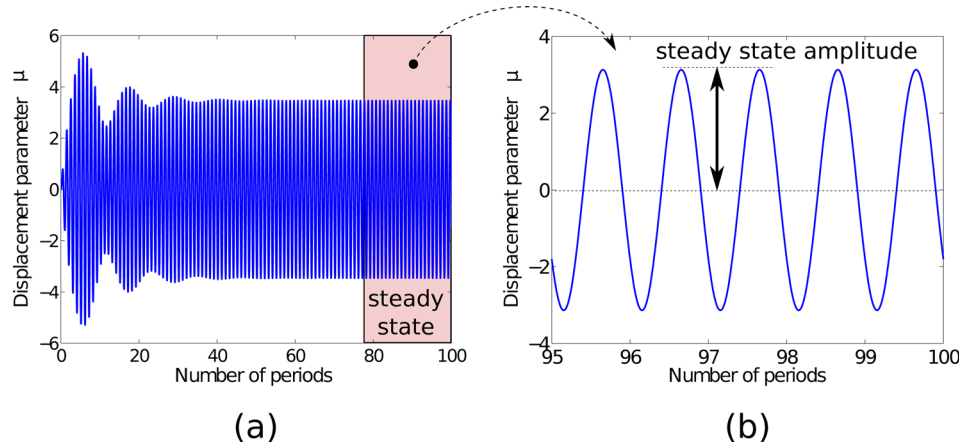


Fig. 21 Numerical response of the equivalent SDOF system (see Sec. 2) (a) and detail of the steady state amplitude used to numerically estimate the energy dissipated per cycle (b)

$$\sigma(t) = \sigma_e(t) + \sigma_m(t) \quad (\text{A2})$$

The reaction in the elastic component is described by the familiar linear material behavior $\sigma_e(t) = E_e \varepsilon(t)$, while the stress in the ductile multilayers is given by

$$\sigma_m(t) = \begin{cases} E_m \varepsilon(t) & \text{if } \varepsilon < \varepsilon_Y \\ E_m \varepsilon_e(t) + E_t \varepsilon_p(t) & \text{if } \varepsilon > \varepsilon_Y \end{cases} \quad (\text{A3})$$

where ε_e , and ε_p , respectively, denote the elastic and plastic component of the displacement field such that, beyond the yield point (ε_Y) $\varepsilon = \varepsilon_e + \varepsilon_p$ (see Fig. 2).

The damping capacity of the model (Q^{-1}) can therefore be computed from the direct numerical solution of Eq. (A1) for forced harmonic motion. Specifically, a fourth-order Runge–Kutta method is used to compute the steady state response $\varepsilon(t) = X \sin(\Omega t + \phi)$ under the effect of a harmonic load $f(t) = F \sin(\Omega t)$ exciting the system at its resonance frequency. From the computed steady state response, shown for clarity in Fig. 21, the elastic and dissipated energies per cycle are computed as

$$\mathcal{U}_{\text{tot}} = \frac{1}{2} (E_m + E_e) X^2 \quad \text{and} \quad \Delta \mathcal{U}_{\text{tot}} = \int_{t_0}^{t_0 + 2\pi/\Omega} f(t) \dot{\varepsilon}(t) dt \quad (\text{A4})$$

from which the loss factor of the system is estimated as in Eq. (1).

References

- [1] Miller, R. A., 1997, "Thermal Barrier Coatings for Aircraft Engines: History and Directions," *J. Therm. Spray Technol.*, **6**(1), p. 3542.
- [2] Evans, A. G., Clarke, D. R., and Levi, C. G., 2008, "The Influence of Oxides on the Performance of Advanced Gas Turbines," *J. Eur. Ceram. Soc.*, **28**(7), pp. 1405–1419.
- [3] Clarke, D. R., Oechsner, M., and Padture, N. P., 2012, "Thermal-Barrier Coatings for More Efficient Gas-Turbine Engines," *MRS Bull.*, **37**(10), pp. 891–898.
- [4] Griffin, J. H., 1990, "A Review of Friction Damping of Turbine Blade Vibration," *Int. J. Turbo Jet Engines*, **7**(3–4), pp. 297–308.
- [5] Limarga, A., Duong, T., Gregori, G., and Clarke, D., 2007, "High-Temperature Vibration Damping of Thermal Barrier Coating Materials," *Surf. Coat. Technol.*, **202**(4), pp. 693–697.
- [6] Gregori, G., Li, L., Nychka, J., and Clarke, D., 2007, "Vibration Damping of Superalloys and Thermal Barrier Coatings at High-Temperatures," *Mater. Sci. Eng., A*, **466**(1), pp. 256–264.
- [7] Patsias, S., Saxton, C., and Shipton, M., 2004, "Hard Damping Coatings: An Experimental Procedure for Extraction of Damping Characteristics and Modulus of Elasticity," *Mater. Sci. Eng., A*, **370**(1), pp. 412–416.
- [8] Patsias, S., Tassini, N., and Lambrinou, K., 2006, "Ceramic Coatings: Effect of Deposition Method on Damping and Modulus of Elasticity for Yttria-Stabilized Zirconia," *Mater. Sci. Eng., A*, **442**(1), pp. 504–508.
- [9] Abu Al-Rub, R. K., and Palazotto, A. N., 2010, "Micromechanical Theoretical and Computational Modeling of Energy Dissipation Due to Nonlinear Vibration of Hard Ceramic Coatings With Microstructural Recursive Faults," *Int. J. Solids Struct.*, **47**(16), pp. 2131–2142.
- [10] Casadei, F., Bertoldi, K., and Clarke, D., 2013, "Finite Element Study of Multi-Modal Vibration Damping for Thermal Barrier Coating Applications," *Comput. Mater. Sci.*, **79**, pp. 908–917.
- [11] Yu, Z., Zhao, H., and Wadley, H. N., 2011, "The Vapor Deposition and Oxidation of Platinum- and Yttria-Stabilized Zirconia Multilayers," *J. Am. Ceram. Soc.*, **94**(8), pp. 2671–2679.
- [12] Begley, M. R., and Wadley, H. N., 2011, "Delamination of Ceramic Coatings With Embedded Metal Layers," *J. Am. Ceram. Soc.*, **94**(s1), pp. s96–s103.
- [13] Begley, M. R., and Wadley, H. N., 2012, "Delamination Resistance of Thermal Barrier Coatings Containing Embedded Ductile Layers," *Acta Mater.*, **60**(6), pp. 2497–2508.
- [14] den Hartog, J. P., 1956, *Mechanical Vibrations*, Dover Publications, New York.
- [15] Hudson, D. E., 1965, "Equivalent Viscous Friction for Hysteretic Systems With Earthquake-Like Excitations," 3rd World Conference on Earthquake Engineering, Auckland/Wellington, New Zealand, January 22–February 1, Vol. 2, pp. 185–201.
- [16] Timoshenko, S., 1951, *Theory of Elasticity*, McGraw-Hill, New York, Vol. 5, p. 500.
- [17] Merker, J., Lupton, D., Topfer, M., and Knake, H., 2001, "High Temperature Mechanical Properties of the Platinum Group Metals," *Platinum Met. Rev.*, **45**(2), pp. 74–82.
- [18] Fischer, B., 2001, "New Platinum Materials for High Temperature Applications," *Adv. Eng. Mater.*, **3**(10), pp. 811–820.
- [19] Torvik, P. J., 2009, "A Slip Damping Model for Plasma Sprayed Ceramics," *ASME J. Appl. Mech.*, **76**(6), p. 061018.
- [20] Reed, S. A., Palazotto, A. N., and Baker, W. P., 2008, "An Experimental Technique for the Evaluation of Strain Dependent Material Properties of Hard Coatings," *Shock Vib.*, **15**(6), pp. 697–712.
- [21] Dahl, P. R., 1976, "Solid Friction Damping of Mechanical Vibrations," *AIAA J.*, **14**(12), pp. 1675–1682.